DOI: 10.65731/ama/2026-0044

acta mechanica et automatica, vol. 20 no. 2 (2026)
Special Issue "Heat and Mass Transfer 2025"

MONITORING THERMAL STRESSES IN HORIZONTAL CYLINDRICAL PRESSURE ELEMENTS

Dawid TALER[*], Marek WĘGLARZ[**], Katarzyna WĘGLARZ[*], Jan TALER[***], Piotr DZIERWA[*]

[*]Faculty of Environmental Engineering and Energy, Department of Thermal Processes, Air Protection and Waste Utilisation, Krakow University of Technology, Warszawska 24, 31-155 Krakow, Poland
[**]Doctoral School, Krakow University of Technology, Warszawska 24, 31-155 Krakow, Poland
[***]Faculty of Environmental Engineering and Energy, Department of Energy, Krakow University of Technology, Jana Pawla II 37, 31-864 Krakow, Poland

dawid.taler@pk.edu.pl, marek.weglarz@doktorant.pk.edu.pl, katarzyna.weglarz@pk.edu.pl, jan.taler@pk.edu.pl, piotr.dzierwa@pk.edu.pl

received 30 January 2026, revised 10 March 2026, accepted 10 March 2026

Abstract: Thermal loading may develop in horizontal boiler components - drums, superheater inlet and outlet headers, and steam lines - when steam condenses on their internal surfaces. The problem is typical for start-ups, shutdowns, and emergency conditions. At start-up, condensate occupies the lower region of the component, whereas steam remains in the upper region. Consequently, the circumferential temperature difference in a horizontal pressure part can become very large, in some cases approaching 200 K, because super-heated steam may heat the upper wall while condensate at saturation temperature cools the lower wall. Such non-uniform heating can produce local plastic deformation, impair drainage, and further intensify thermal stresses; deformed superheater headers are a frequent practical example. This study develops an inverse heat conduction procedure for reconstructing the temperature field in the cross-section of a horizontal pressure element. The reconstructed field is then used in a finite element analysis to calculate transient thermal stresses. The component is assumed to be externally insulated, and equally spaced thermocouples are placed inside the wall near the inner surface. Numerical tests are carried out for several numbers of measurement locations distributed over half of the circumference, with detailed results reported for 7, 13, and 19 points. The temperature field between the outer surface and the thermocouple radius is obtained from a direct heat conduction solution. The temperature and heat-flux histories at the thermocouple radius are then used as input for the inverse analysis, which provides both the inner-wall temperature and the local heat transfer coefficient in the steam and condensate zones.

Keywords: horizontal pressure elements, finite volume method, inverse heat conduction problem, heat transfer coefficient

1. INTRODUCTION

Allowable heating and cooling rates for thick-walled boiler pressure parts, together with environmental emission constraints at different boiler loads for a $350 \cdot 10^3$ kg/h steam flow rate, were analysed in [1]. The operational flexibility and emissions of gas- and coal-fired units, including nitrogen oxides, sulphur dioxide, and carbon dioxide, were reviewed in [2] with particular attention to future power systems with a high share of renewable energy.

Skjervold and Nord [3] proposed a steam accumulator for a 598 MW unit with post-combustion CO_2 capture as a means of improving operating flexibility. In a related study, Skjervold et al. [4] examined control concepts for adsorption-based CO_2 capture under varying boiler load. Pressurised hot-water storage tanks and steam accumulators as flexibility-enhancing devices for thermal power plants were analysed by Trojan et al. [5] and Stevanovic et al. [6]. These studies show that a reliable assessment of thermal stresses in critical pressure parts is a prerequisite for flexible, safe plant operation. Stress information is also required when the temperature history of the working fluid is optimised during heating or cooling, because the permissible rate of change must be selected so that the allowable stress is not exceeded.

In horizontal pressure parts of conventional power units [7-9], and also in nuclear installations [10], start-ups and shutdowns may generate severe thermal stresses because water and steam can coexist in the same cross-section. Condensate occupies the lower portion of the element, while steam, frequently superheated, flows above it. The wall is therefore exposed to highly non-uniform circumferential heating, since the heat transfer coefficients in the water and steam regions differ markedly. In conventional plants, boiler drums, superheater inlet and outlet headers, and steam-cooler headers are particularly vulnerable to such loads. In pressurised-water reactors, comparable circumferential temperature gradients may occur near horizontal reactor inlet nozzles. Boiler codes [11] usually neglect this circumferential asymmetry and treat the wall temperature field as axisymmetric. Thermal-stress calculations in conventional and nuclear pressure components commonly assume known values of the heat transfer coefficient and fluid temperature [12]. However, both quantities are difficult to measure accurately in high-pressure, high-velocity, high-temperature flows, where dynamic temperature-measurement errors can be substantial [8].

The present work formulates a procedure for reconstructing the temperature field in an externally insulated horizontal pressure element. The input consists of wall-temperature histories measured around the circumference at a small distance from the inner surface. From these data, the transient temperature distribution in the

DOI: 10.65731/ama/2026-0044

complete cross-section is obtained. When the internal fluid temperature is also available, the circumferential distribution of the heat transfer coefficient on the inner surface can be evaluated. This coefficient is then used as a boundary condition in finite element calculations of thermal stresses in the pressure element.

2. MATHEMATICAL FORMULATION OF THE DIRECT PROBLEM

The transient temperature field in the horizontal pressure element is governed by the heat conduction equation:

$$c(T)\rho(T)\ \frac{\partial T}{\partial t} = \frac{1}{r}\frac{\partial}{\partial r}\left[rk(T)\frac{\partial T}{\partial r}\right] + \frac{1}{r}\frac{\partial}{\partial \varphi}\left[\frac{k(T)}{r}\frac{\partial T}{\partial \varphi}\right] \quad (1)$$

boundary conditions:

$$\left[k(T)\frac{\partial T}{\partial r}\right]\Big|_{r=r_{in}} = h_w\left[T|_{r=r_{in}} - T_w(t)\right] \quad 0 \le \varphi \le \gamma(t) \quad (2)$$

$$\left[k(T)\frac{\partial T}{\partial r}\right]\Big|_{r=r_{in}} = h_s\left[T|_{r=r_{in}} - T_s(t)\right] \quad \gamma(t) < \varphi \le \pi \quad (3)$$

$$\left[k(T)\frac{\partial T}{\partial r}\right]\Big|_{r=r_{out}} = 0 \qquad 0 \le \varphi \le \pi \quad (4)$$

and initial condition:

$$T|_{t=t_0} = T_0(r.\varphi) \quad (5)$$

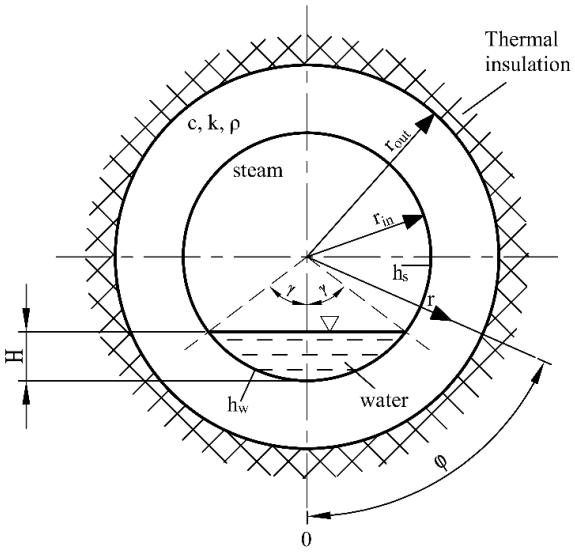

Fig. 1. Cross-section of a horizontal cylindrical header; steam flows through the upper part of the header, and condensate collects in the lower part

During heating, saturated dry steam enters the header. Initially, the internal wall surface is much colder than the incoming steam, so condensation occurs and liquid collects in the lower part of the horizontal header. The maximum condensate height is denoted by H (Fig. 1). The heat transfer coefficient in the steam region, h_s, is much larger than the coefficient in the water region, h_w. In the direct heat conduction problem, the inner-surface boundary conditions (1)-(3), the outer-surface boundary condition (4), and the initial condition (5) are prescribed. The resulting initial-boundary-value problem (1)-(5) is solved with the finite volume method (FVM) [13]. Figure 2 shows the discretisation of half of the header cross-section into control volumes. The circumferential direction is represented by N uniformly spaced nodes, whereas the radial direction is represented by M nodes; hence the transient wall temperature is calculated at M x N nodal points.

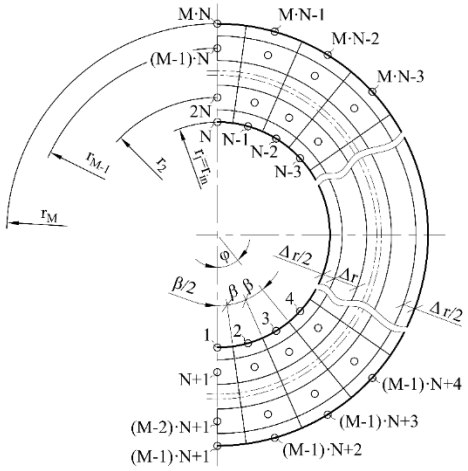

Fig. 2. Division of half of the cross-section of a cylindrical element into finite volumes

For each control volume, a heat-balance equation is written to obtain the transient temperature at each node. Representative balances are given below for a node on the internal surface, a node within the wall, and a node on the external surface. For the i-th node on the inner surface of the header (Fig. 3), the balance takes the following form:

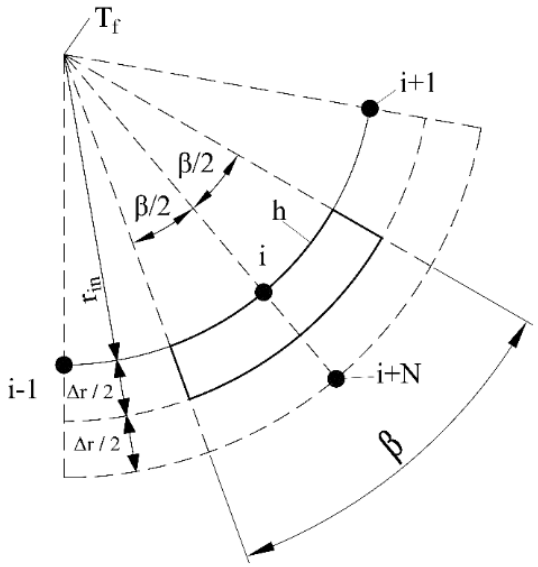

Fig. 3. Diagram illustrating the heat balance equation for the i-th node on the inner surface of the header

$$\beta\frac{1}{2\pi}\pi\left[\left(r_{in}+\frac{\Delta r}{2}\right)^2 - r_{in}^2\right]c(T_i)\,\rho(T_i)\,\frac{dT_i}{dt}$$
$$= \frac{k(T_{i-1})+k(T_i)}{2}\cdot\frac{\Delta r}{2}\cdot\frac{T_{i-1}-T_i}{\beta\cdot r_{in}} + \frac{k(T_{i+1})+k(T_i)}{2}\cdot\frac{\Delta r}{2}\cdot\frac{T_{i+1}-T_i}{\beta\cdot r_1} \quad (6)$$
$$+ \frac{k(T_i)+k(T_{i+N})}{2}\cdot\frac{\beta(r_1+r_2)}{2}\cdot\frac{T_{i+N}-T_i}{\Delta r} + \alpha_i\beta\, r_{in}(T_f - T_i)$$

Equation (6) can be written in the following form:

$$\frac{dT_i}{dt} = \frac{2\kappa(T_i)}{\beta\Delta r\left(r_{in}+\frac{\Delta r}{4}\right)}\left[\frac{\Delta r}{2\beta\cdot r_{in}}\frac{k(T_{i-1})+k(T_i)}{2k(T_i)}(T_{i-1}-T_i)+\right.$$

$$\frac{\Delta r}{2\beta\cdot r_{in}}\frac{k(T_{i+1})+k(T_i)}{2k(T_i)}(T_{i+1}-T_i)+ \quad (7)$$

$$\left.\frac{\beta(r_1+r_2)}{2\Delta r}\frac{k(T_{i+N})+k(T_i)}{2k(T_i)}(T_{i+N}-T_i)+\beta Bi_i(T_f-T_i)\right]$$

$$i = 2.\ldots.(N-1)$$

where the symbol $Bi_i = h_i r_{in}/k(T_i)$ stands for the Biot number for every *i*-th node.

The balance for node (*j*-1)*N*+*i*, located inside the wall, is derived next (Fig. 4).

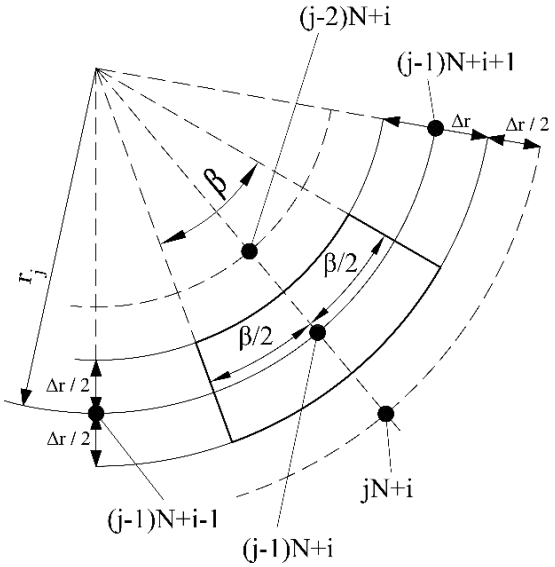

Fig. 4. Diagram illustrating the heat balance equation for node (*j*-1)*N*+*I*, *i*=2. … .(*N*-1) ; *j*=2. … .(*M*-1) located inside the header wall

For an internal node, with *i* = 2, … , *N*-1 and *j* = 2, … , *M*-1, the heat-balance equation is:

$$\beta r_j \Delta r\, c(T_{(j-1)N+i})\cdot\rho(T_{(j-1)N+i})\cdot\frac{dT_{(j-1)N+i}}{dt}$$

$$= \frac{k(T_{(j-1)N+i-1})+k(T_{(j-1)N+i})}{2}\cdot\Delta r\cdot\frac{T_{(j-1)N+i-1}-T_{(j-1)N+i}}{\beta\cdot r_j}$$

$$+\frac{k\left(T_{(j-1)N+i+1}\right)+k(T_{(j-1)N+i})}{2}\cdot\Delta r\cdot\frac{T_{(j-1)N+i+1}-T_{(j-1)N+i}}{\beta\cdot r_j} \quad (8)$$

$$\frac{k\left(T_{(j-2)N+i}\right)+k(T_{(j-1)N+i})}{2}\cdot\beta\frac{r_{j-1}+r_j}{2}\cdot\frac{T_{(j-2)N+i}-T_{(j-1)N+i}}{\Delta r}$$

$$\frac{k\left(T_{(jN+i)}\right)+k(T_{(j-1)N+i})}{2}\cdot\beta\frac{r_{j+1}+r_j}{2}\cdot\frac{T_{jN+i}-T_{(j-1)N+i}}{\Delta r}$$

Equation (8) can be written in the following form:

$$\frac{dT_{(j-1)N+i}}{dt} =$$

$$\frac{\kappa\left(T_{(j-1)N+i}\right)}{\beta\, r_j\,\Delta r}\left[\frac{\Delta r}{\beta\, r_j}\frac{k\left(T_{(j-1)N+i-1}\right)+k\left(T_{(j-1)N+i}\right)}{2k\left(T_{(j-1)N+i}\right)}\left(T_{(j-1)N+i-1}-T_{(j-1)N+i}\right)+\right.$$

$$\frac{\Delta r}{\beta\cdot r_j}\frac{k\left(T_{(j-1)N+i+1}\right)+k\left(T_{(j-1)N+i}\right)}{2k\left(T_{(j-1)N+i}\right)}\left(T_{(j-1)N+i+1}-T_{(j-1)N+i}\right)+$$

$$\frac{\beta(r_{j-1}+r_j)}{2\Delta r}\frac{k\left(T_{(j-2)N+i}\right)+k\left(T_{(j-1)N+i}\right)}{2k\left(T_{(j-1)N+i}\right)}\left(T_{(j-2)N+i}-T_{(j-1)N+i}\right)+$$

$$\left.\frac{\beta\,(r_{j+1}+r_j)}{2\Delta r}\frac{k\left(T_{(jN+i)}\right)+k\left(T_{(j-1)N+i}\right)}{2k\left(T_{(j-1)N+i}\right)}\left(T_{jN+i}-T_{(j-1)N+i}\right)\right] \quad (9)$$

i=2. … .(*N*-1)

j=2. ….(*M*-1)

Figure 5 defines the numbering used when writing the heat-balance equation for the thermally insulated external surface of the header.

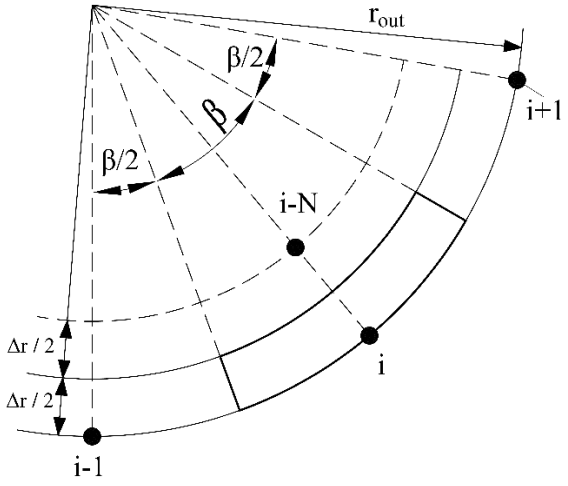

Fig. 5. Diagram illustrating the heat balance for the *i*-th node on the outer surface of the header

For the outer-surface nodes numbered from *i* = [(*M*-1)*N*+2] to *i* = (*M* x *N* - 1), the heat balance shown in Fig. 5 is written as:

$$\frac{\boldsymbol{\beta}}{\mathbf{2}}\left[\boldsymbol{r_{out}^2}-\left(\boldsymbol{r_{out}}-\frac{\boldsymbol{\Delta r}}{\mathbf{2}}\right)^{\mathbf{2}}\right]\boldsymbol{c(T_i)}\,\boldsymbol{\rho(T_i)}\,\frac{\boldsymbol{dT_i}}{\boldsymbol{dt}}$$

$$= \frac{k(T_{i-1})+k(T_i)}{2}\,\frac{\Delta r}{2}\,\frac{T_{i-1}-T_i}{\beta\, r_{out}}+\frac{k(T_{i+1})+k(T_i)}{2}\,\frac{\Delta r}{2}\,\frac{T_{i+1}-T_i}{\beta\, r_{out}} \quad (10)$$

$$+\frac{k(T_{i-N})+k(T_i)}{2}\,\frac{\beta(r_{M-1}+r_M)}{2}\,\frac{T_{i-N}-T_i}{\Delta r}$$

After rearrangement, equation (10) becomes:

$$\frac{dT_i}{dt} = \frac{2\kappa(T_i)}{\beta\,\Delta r\left(r_{out}-\frac{\Delta r}{4}\right)}\left[\left(\frac{k(T_{i-1})+k(T_i)}{2k(T_i)}\frac{\Delta r}{2\,\beta\, r_{out}}(T_{i-1}-T_i)+\right.\right.$$

$$\frac{k(T_{i+1})+k(T_i)}{2k(T_i)}\frac{\Delta r}{2\,\beta\, r_{out}}(T_{i+1}-T_i)+ \quad (11)$$

$$\left.\left.\frac{k(T_{i-N})+k(T_i)}{2k(T_i)}\frac{\beta(r_{M-1}+r_M)}{2\,\Delta r}(T_{i-N}-T_i)\right]\right.$$

$$i = (M-1)N+2\ldots(M\cdot N-1)$$

A system of (*M*·*N*) first-order differential equations was solved using the fourth-order Runge-Kutta method. The solutions to the system of equations are the temperatures of the header wall at the nodes. Changes in the internal surface temperature around the

DOI: 10.65731/ama/2026-0044

header circumference are determined based on the circumferential temperature distribution measured at a distance Δr from the internal surface. By determining the temperature distribution in the immediate area: (r_{in} - Δr) ≤ r ≤(r_{out} - Δr), 0 ≤φ ≤ π, the circumferential temperature distribution and heat flux at the radius r = r_{in} + Δr can be determined. Then, the inverse heat conduction problems in the area r_{in} ≤ r ≤ (r_{in} + Δr), 0 ≤ φ ≤ π are solved. The solution to the inverse problem yields the circumferential distribution of the internal header surface temperature: $T(r_{in}\ \varphi)$. After determining the temperature distribution across the entire cross-section of the header, the thermal stress distribution can then be determined using the finite element method (FEM). The accuracy of the proposed method for monitoring thermal stresses will be evaluated through computational tests. The 'measurement data' will be generated from the direct solution of the heat conduction problem, in which it is assumed that the temperature of the medium inside the header and the circumferential distribution of the HTC on the inner surface of the header are known. This will yield the measurement data $T_m(r_{in} + \Delta r.\ \varphi_j)$ and heat flux: $\dot{q}_m(r_{in} + \Delta r.\ \varphi_j)$.

Tab. 1. Thermal conductivity coefficient and thermal diffusivity of P91 steel as a function of temperature [14]

Temperature, °C	**20**	**100**	**200**	**300**	**400**	**500**	**600**
Thermal conductivity coefficient k, W/(m·K)	28.7	29	29.6	29.7	29.7	29.6	29.3
Thermal diffusivity, $\kappa \cdot 10^6$ m²/s	8.27	7.70	7.30	6.78	6.18	5.43	4.70

The direct and inverse calculations are presented for a header made of P91 ferritic-martensitic steel. The temperature-dependent thermal conductivity and diffusivity of this material are listed in Table 1. The inner radius is 0.1275 m, and the wall thickness is 0.05 m. The angle gamma in Fig. 1 is 37.5 degrees; therefore, the heat transfer coefficient was set to 1000 W/(m² K) at nodes 1-3 and to 3000 W/(m² K) in the steam space. The higher coefficient in the steam region reflects condensation of saturated steam on a wall whose temperature is initially lower than the steam temperature. The transient calculations assume an initial wall temperature of 20 degrees Celsius and a steam temperature of 100 degrees Celsius. The mesh contains N = 13 nodes in the circumferential direction and M = 11 nodes in the radial direction. A time step of Δt = 1 s was used in the fourth-order Runge-Kutta integration.

3. MATHEMATICAL FORMULATION OF THE INVERSE PROBLEM

In the inverse problem, we know the temperature measurements at nodes numbered from N+1 to 2N. Considering that the outer surface of the header is thermally insulated, the temperature in the area $r_2 \le r \le r_M, 0 \le \varphi < \pi$ is determined from the solution of the direct problem. As a result of solving the direct problem, the temperatures in all nodes from (N+1) to (M·N) are known. To solve the inverse problem, it is necessary to know the measured temperatures on the radius r_2, i.e., in nodes from (N+1) to 2N, and the temperatures in nodes on the radius r_3 determined from the solution of the direct problem. These are nodes from (2N+1) to 3N. The angular pitch $\Delta\varphi$ between the temperature measurement points is $\Delta\varphi = \pi/(N-1)$.

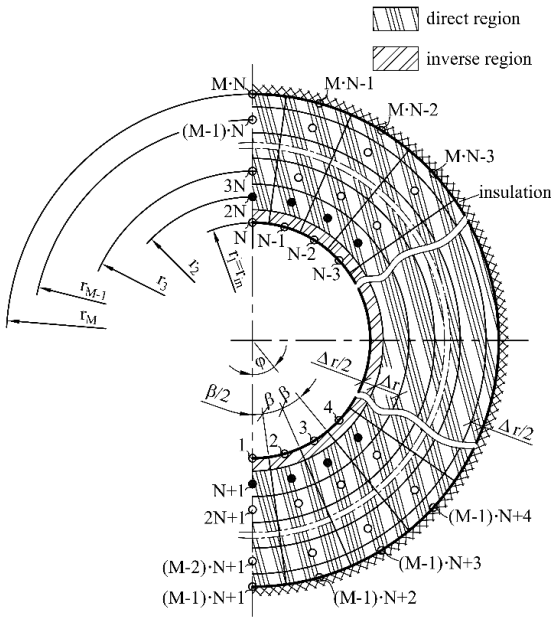

Fig. 6. Division of half of the cross-section of a cylindrical element into finite volumes in the inverse problem; nodes located on the radius $\boldsymbol{r_2}$, where the wall temperature is measured

The heat-balance equations written for nodes N+1 to 2N are used to evaluate the temperatures at the inner-surface nodes 1 to N.

– heat-balance equation for node N+1

$$\frac{\boldsymbol{\beta}}{\mathbf{2}}\ \boldsymbol{r_2}\ \Delta\boldsymbol{r_c}\ (\boldsymbol{T_{N+1}})\ \boldsymbol{\rho}\ (\boldsymbol{T_{N+1}})\ \frac{\boldsymbol{dT_{N+1}}}{\boldsymbol{dt}} =$$
$$\frac{\beta}{2}\ \frac{r_{in}+r_2}{2}\ \frac{k(T_1)+k(T_{N+1})}{2}\ \frac{T_1-T_{N+1}}{\Delta r} \tag{12}$$
$$+\frac{\beta}{2}\ \frac{r_2+r_3}{2}\ \frac{k(T_{N+1})+k(T_{2N+1})}{2}\ \frac{T_{N+1}-T_{2N+1}}{\Delta r}$$
$$+\Delta r\ \frac{k(T_{N+1})+k(T_{N+2})}{2}\ \frac{T_{N+1}-T_{2N+1}}{\beta\ r_2}$$

– equation (12) is used to determine the temperature T_1:

$$T_1 = T_{N+1} + \frac{4\ r_2\ (\Delta r)^2}{(r_{in}+r_2)}\ \frac{1}{\kappa(T_{N+1})} - \frac{k\ (T_{N+1})}{k(T_{N+1})+k(T_1)}\ \frac{dT_{N+1}}{dt}$$
$$-\frac{(r_2+r_3)}{(r_{in}+r_2)}\ \frac{k(T_{N+1})+k(T_{2N+1})}{k(T_{N+1})+k(T_1)}(T_{2N+1}-T_{N+1}) \tag{13}$$
$$-\frac{4(\Delta r)^2}{\beta^2(r_{in}+r_2)\ r_2}\ \frac{k(T_{N+1})+k(T_{N+2})}{k(T_{N+1})+k(T_1)}\ (T_{N+2}-T_{N+1})$$

– heat balance equations for nodes (N+i. i=2. …. 2N-1) located at a distance Δr from the inner surface; these are equations for nodes N+2. …. 2N-1

$$\frac{\beta}{2}\ r_2\ \Delta r\ \frac{1}{\kappa(T_{N+i})}\ \frac{dT_{N+i}}{dt} =$$
$$\frac{\beta\ (r_1+r_2)}{2\ \Delta r}\ \frac{k(T_{N+i})+k(T_i)}{2\ k\ (T_{N+i})}\ (T_i - T_{N+i})$$
$$+\ \frac{\beta\ (r_2+r_3)}{2\ \Delta r}\ \frac{k(T_{N+i})+k(T_{2N+i})}{2\ k\ (T_{N+i})}\ (T_{2N+i} - T_{N+i})$$

$$+\frac{\Delta r}{\beta\, r_2}\,\frac{k(T_{N+i})+k(T_{N+i-1})}{2\,k\,(T_{N+i})}\,(T_{N+i-1}-T_{N+i}) \quad (14)$$

$$+\frac{\Delta r}{\beta\, r_2}\,\frac{k(T_{N+i})+k(T_{N+i+1})}{2\,k\,(T_{N+i})}\,(T_{N+i+1}-T_{N+i})$$

$$i=2.\ldots.N-1$$

– solving equation (14) provides the expression used to calculate the temperatures of the internal-surface nodes numbered from 2 to *N*-1.

$$T_i = T_{N+i} + \frac{2\,r_2\,(\Delta r)^2}{(r_{in}+r_2)}\,\frac{2\,k\,(T_{N+i})}{k(T_{N+i})+k(T_i)}\,\frac{1}{\kappa\,(T_{N+i})}\,\frac{dT_{N+i}}{dt}$$
$$-\frac{r_2+r_3}{r_{in}+r_2}\,\frac{k(T_{N+i})+k(T_{2N+i})}{k\,(T_{N+i})+k(T_i)}\,(T_{2N+i}-T_{N+i})$$
$$-\frac{2\,(\Delta r)^2}{\beta^2 r_2(r_{in}+r_2)}\,\frac{k(T_{N+i})+k(T_{N+i-1})}{k\,(T_{N+i})+k\,(T_i)}\,(T_{N+i-1}-T_{N+i}) \quad (15)$$
$$-\frac{2\,(\Delta r)^2}{\beta^2 r_2(r_{in}+r_2)}\,\frac{k(T_{N+i})+k(T_{N+i+1})}{k\,(T_{N+i})+k\,(T_i)}\,(T_{N+i+1}-T_{N+i})$$

$$i=2.\ldots.N-1$$

– heat balance equation for node 2N

$$\frac{\beta\, r_2\,\Delta r}{2}\,\frac{1}{\kappa(T_{2N})}\,\frac{dT_{2N}}{dt}=$$
$$\frac{\beta(r_{in}+r_2)}{4\,\Delta r}\,\frac{k(T_{2N})+k(T_N)}{2\,k\,(T_{2N})}\,(T_N-T_{2N})$$
$$+\frac{\beta\,(r_2+r_3)}{4\,\Delta r}\,\frac{k(T_{2N})+k(T_{3N})}{2\,k\,(T_{2N})}\,(T_{3N}-T_{2N}) \quad (16)$$
$$+\frac{\Delta r}{\beta\, r_2}\,\frac{k(T_{2N-1})+k(T_{2N})}{2\,k\,(T_{2N})}\,(T_{2N-1}-T_{2N})$$

– by solving equation (16) for T_N, we obtain:

$$T_N = T_{2\,N} + \frac{2\,r_2\,(\Delta r)^2}{(r_{in}+r_2)}\,\frac{2\,k\,(T_{2\,N})}{k(T_{2\,N})+k(T_N)}\,\frac{1}{\kappa\,(T_{2\,N})}\,\frac{dT_{2\,N}}{dt}$$
$$-\frac{r_2+r_3}{r_{in}+r_2}\,\frac{k(T_{2N})+k(T_{3N})}{k\,(T_{2N})+k(T_N)}\,(T_{3N}-T_{2N}) \quad (17)$$
$$-\frac{4\,(\Delta r)^2}{\beta^2 r_2(r_{in}+r_2)}\,\frac{k(T_{2\,N-1})+k(T_{2\,N})}{k\,(T_N)+k\,(T_{2\,N})}\,(T_{2\,N-1}-T_{2\,N})$$

If the time variation of the fluid temperature $T_f(t)$ is also known from the measurement, the distribution of the HTC on the inner surface of the header can be determined.

The HTC h_i on the inner surface of the header is determined using the following formula:

$$h_i=\frac{\dot{q}_i}{T_f-T_i}\quad i=1.\ldots N \quad (18)$$

where: $\dot{q}_i$ - heat flux at node *i*. T_f average mass temperature of the fluid in the header. T_i - temperature on the inner surface of the header at node *i*.

The heat flux $\dot{q}_i$ at nodes *i* =1. … .*N* is determined using the formula:

$$\dot{q}_i=-k(T_i)\,\frac{\partial T(r.\varphi)}{dr}\,|r_i.\varphi_i \cong k(T_i)\,\frac{3T_i-4T_{N+i}+T_{2N+i}}{2\Delta r} \quad (19)$$

The derivative with respect to the radius in formula (19) for $\partial T/dr$ was approximated by the forward difference quotient with second-order accuracy.

4. COMPUTATION RESULTS

This section presents the numerical results for the direct and inverse heat conduction analyses.

4.1. Tmperature field in the horizontal-header cross-section – direct heat conduction problem

The following subsection discusses the transient temperature field obtained for the horizontal header, given the boundary and initial conditions. These direct-problem input data were specified at the end of Section 2. Figures 7 and 8 show the transient temperature distributions on the internal and external header surfaces at selected times.

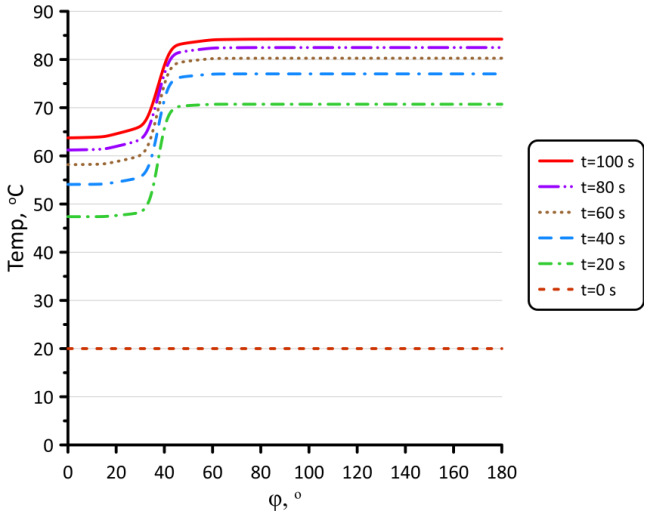

Fig. 7. Temperature distribution around the inner surface of the header at selected time points

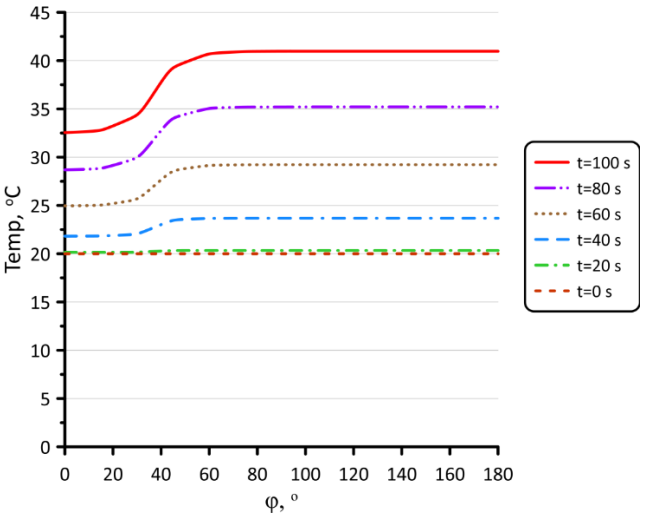

Fig. 8. Temperature distribution around the outer surface of the header at selected time points

DOI: 10.65731/ama/2026-0044

The analysis of the results presented in Figures 7 and 8 shows that the temperature of the inner surface of the header rises faster than the temperature of the outer surface. The temperature difference across half the header circumference is significantly greater on the inner surface than on the outer surface. The temperature differences around the header circumference are caused by different HTC in the areas where condensate and steam are present simultaneously. The radial temperature distribution for angles φ = 0 (water area) and $\varphi = \pi$ (steam area) is shown in Figures 9 and 10, respectively.

Figures 9 and 10 show that the lower part of the header warms up more slowly because the water-containing region has the lower HTC. The FVM temperatures obtained in this work were compared with results generated in Ansys. The three-dimensional temperature and stress analyses were carried out for a sufficiently long header segment so that the ends did not influence the stress state at mid-length. The model allowed free elongation and bending of the header. Several finite-element discretisations were analysed to verify mesh independence.

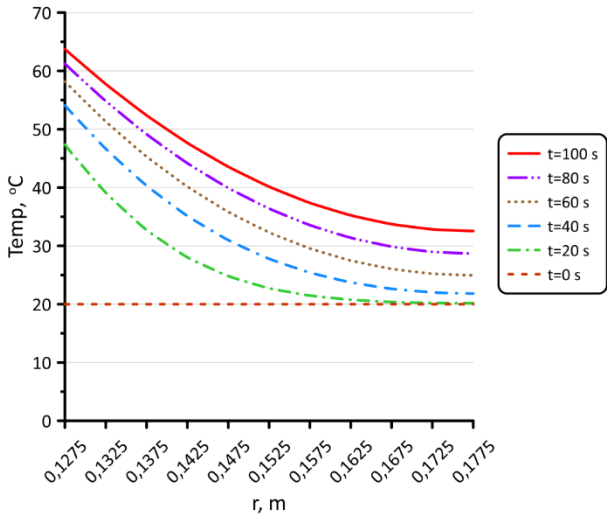

Fig. 9. Radial temperature distribution in the header wall for selected time points $\boldsymbol{\varphi = 0°}$ (water area)

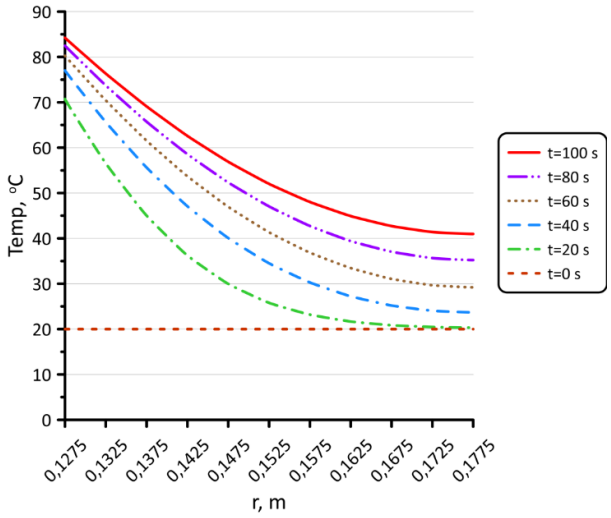

Fig. 10. Radial temperature distribution in the header wall for selected time moments. $\boldsymbol{\varphi = \pi}$ (steam area)

The FVM temperature histories calculated 5 mm from the inner surface were used as artificial measurement data. Figure 11 indicates very good agreement between the wall temperatures obtained by FVM and by FEM in Ansys.

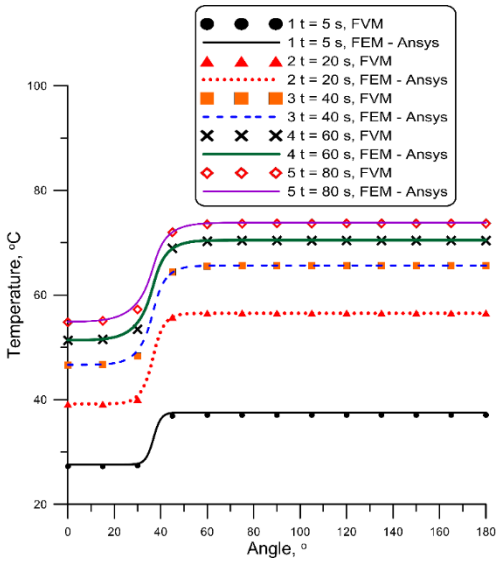

Fig. 11. Comparison of the header wall temperature at a distance of 5 mm from the inner surface determined using the finite volume method (FVM) and the finite element method (FEM)

4.2. Evaluation of the inverse-problem results

The inverse solution was used to reconstruct the header's inner-surface temperature. Temperatures at nodes N+1 to 2N, calculated by FVM and shown in Fig. 11, served as inverse-problem input data. Temperatures at nodes 2N+1 to 3N were also obtained from the FVM direct solution and are shown in Fig. 12.

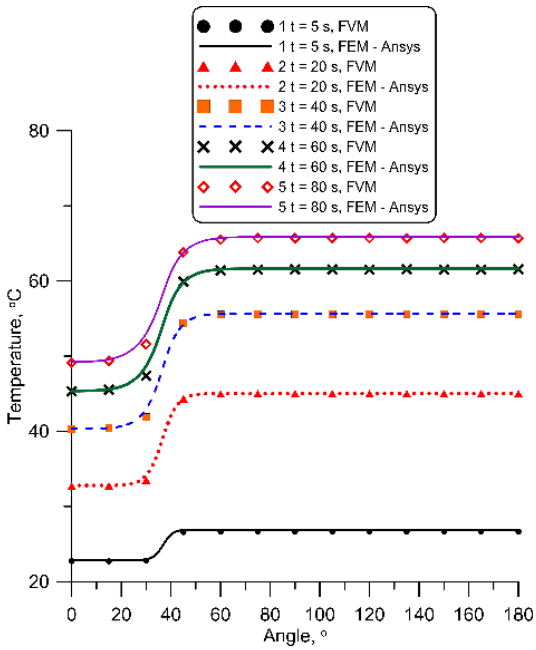

Fig. 12. Temperature of the header wall at a distance of 10 mm from the inner surface obtained from the solution of the direct problem using FVM and FEM, calculated by Ansys

Figure 12 confirms that the FVM and FEM temperature predictions are nearly the same.

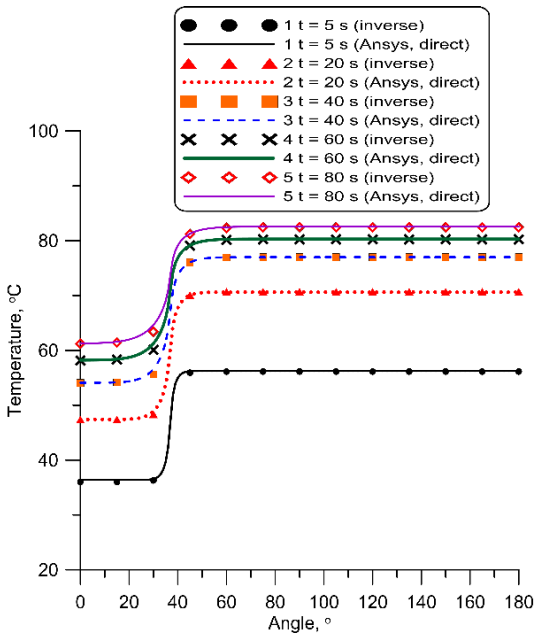

Fig. 13. Comparison of the internal header surface temperature determined from the inverse problem solution with input data determined using FEM

The inner-surface temperature obtained from the inverse heat conduction analysis was compared with the temperature calculated in Ansys (Fig. 13). The agreement is very close. Figure 14 compares the heat transfer coefficients recovered by the proposed inverse procedure with the input values used in the direct calculation. For the third-kind boundary condition imposed on the inner surface, the HTC was set to 1000 W/(m^2 K) for the angular interval from 0 degrees to 37.5 degrees and to 3000 W/(m^2 K) for the interval from 37.5 degrees to 180 degrees.

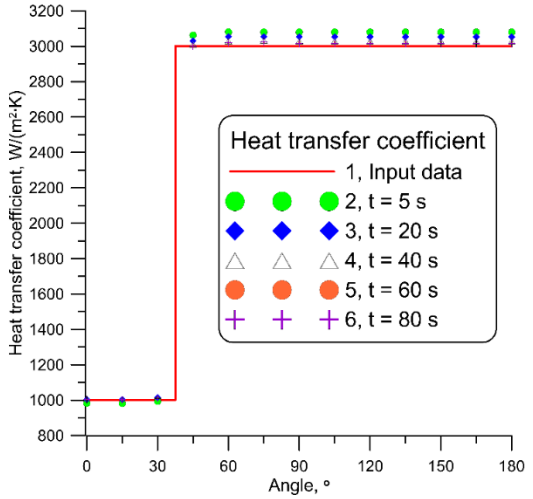

Fig. 14. Changes in the HTC on half of the inner surface of the header; 1 specified (exact) changes in the HTC; 2, 3, 4, 5, and 6 – changes in the HTC determined from the inverse problem solution for times 5, 20, 40, 60, and 80 seconds, respectively

To quantify the accuracy of the reconstructed inner-surface HTC, relative differences between the values obtained from the inverse heat conduction solution and the prescribed input data were calculated as follows:

$$\varepsilon_{h,i} = \frac{h_i^{inverse} - h_i^{input}}{h_i^{input}} \cdot 100\% \tag{20}$$

Tab. 2. Comparison of the HTC on the inner surface of the header determined from the inverse heat conduction problem with HTC values adopted for solving the direct problem (input data)

Angle, °	t = 5 s	t = 20 s	t = 40 s	t = 60 s	t = 80 s
0	-1.66	0.43	0.36	0.24	0.41
15	-1.76	0.52	0.37	0.17	0.36
30	-0.56	1.52	1.25	1.33	1.06
45	2.09	1.03	0.36	0.11	-0.02
60	2.69	1.83	1.00	0.68	0.67
75	2.67	1.83	1.14	0.77	0.81
90	2.67	1.78	1.01	0.78	0.55
105	2.67	1.78	1.01	0.78	0.52
120	2.67	1.78	1.01	0.78	0.52
135	2.67	1.78	1.01	0.78	0.52
150	2.67	1.78	1.01	0.78	0.52
165	2.67	1.78	1.01	0.78	0.52
180	2.67	1.78	1.01	0.78	0.52

The results of the relative differences $\varepsilon_{h,i}$ calculations are summarised in Table 2. Inspection of the results in Table 2 shows that the proposed method provides very good accuracy in determining HTC. The largest differences $\varepsilon_{h,i}$ occur at a time of 5 seconds, but do not exceed 2.67%. In the following time points, the differences $\varepsilon_{h,i}$ are significantly smaller.

4.3. Thermal stress analysis

The temperature distributions obtained in the direct and inverse regions were used to calculate the stress field in the header cross-section. The header ends were assumed to be free to elongate and bend. Temperature and stress results are presented in a section located 4 m from the free end. Additional tests were performed to evaluate the influence of FEM mesh density on the results.

Three meshes with different radial, circumferential, and axial resolutions were considered. The calculations used the following finite-element meshes:

- Mesh number 1 - 5 x 45 x 50
- Mesh number 2 - 10 x 90 x 100
- Mesh number 3 - 20 x 180 x 200

The first number in the grid designation indicates the number of elements in the radial direction. The second number indicates the number of elements in the circumferential direction on half of the circumference, and the third number indicates the number of elements in the axial direction. A comparison of the temperatures calculated at point (r_{in}. 0) at the bottom of the header and at point (r_{in}. π) at the top of the header using the Ansys program is presented in Table 3.

DOI: 10.65731/ama/2026-0044

Tab. 3. Comparison of temperatures in °C at point (r=rin. φ=0) and at point (r=r_{in}. φ = π). It was assumed that for an angle of 0° ≤ φ ≤ 37.5° , the HTC is 1000 W/(m² K), while for an angle of 37.5°≤ φ ≤ 142.5°, HTC is 3000 W/(m² K)

Times	Mesh no. 1		Mesh no. 2		Mesh no. 3	
	$r = r_{in}. \varphi = \pi$	$r = r_{in}. \varphi = 0$	$r = r_{in}. \varphi = \pi$	$r = r_{in}. \varphi = 0$	$r = r_{in}. \varphi = \pi$	$r = r_{in}. \varphi = 0$
5.5	57.331	37.063	57.31	37.053	57.309	37.053
10	63.722	41.527	63.727	41.529	63.728	41.53
20	70.604	47.404	70.609	47.407	70.61	47.407
40	76.988	54.088	76.991	54.091	76.992	54.091
60	80.306	58.218	80.308	58.221	80.308	58.22
80	82.558	61.285	82.56	61.292	82.56	61.288
100	84.338	63.832	84.34	63.843	84.34	63.837

The analysis of the results presented in Table 3 shows that the calculations for mesh no. 2 achieve satisfactory accuracy. Radial, circumferential, and longitudinal stresses were determined using the finite element mesh no. 2. Fig. 15 shows the time-dependent temperature differences on the inner surface between angle $\varphi = \pi$ (top of the header) and angle $\varphi = 0$ (bottom of the header).

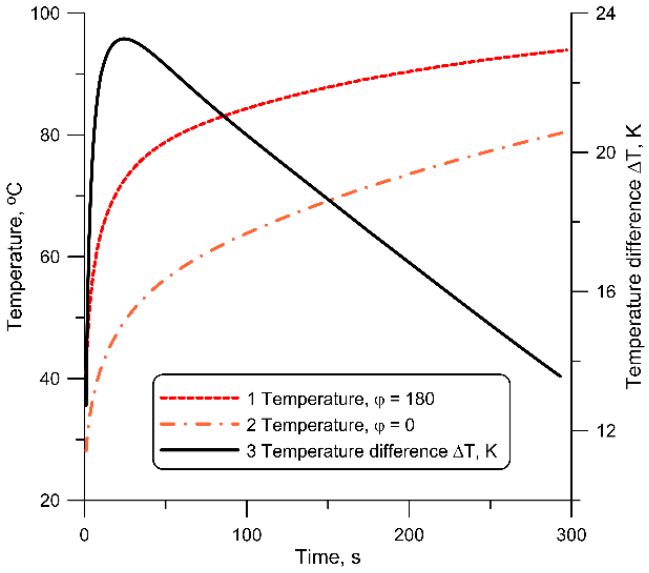

Fig. 15. The temperature difference ΔT between the highest and lowest points located on the inner surface of the header

The top-to-bottom inner-surface temperature difference was evaluated as:

$$\Delta T = T(r_{in}, \pi) - T(r_{in}, 0) \tag{21}$$

The temperature difference between the upper and lower regions results from the different HTCs. The upper region, swept by condensing steam, becomes hotter and is associated here with an HTC of 3000 W/(m² K). The lower region heats more slowly because its HTC is 1000 W/(m² K). The temperature difference ΔT reaches a maximum of 23.26 K at t = 25 s. After this peak, ΔT decreases as the header approaches thermal equilibrium.

Representative temperature and stress distributions at t = 20 s are shown in Figs. 16(a)-16(d).

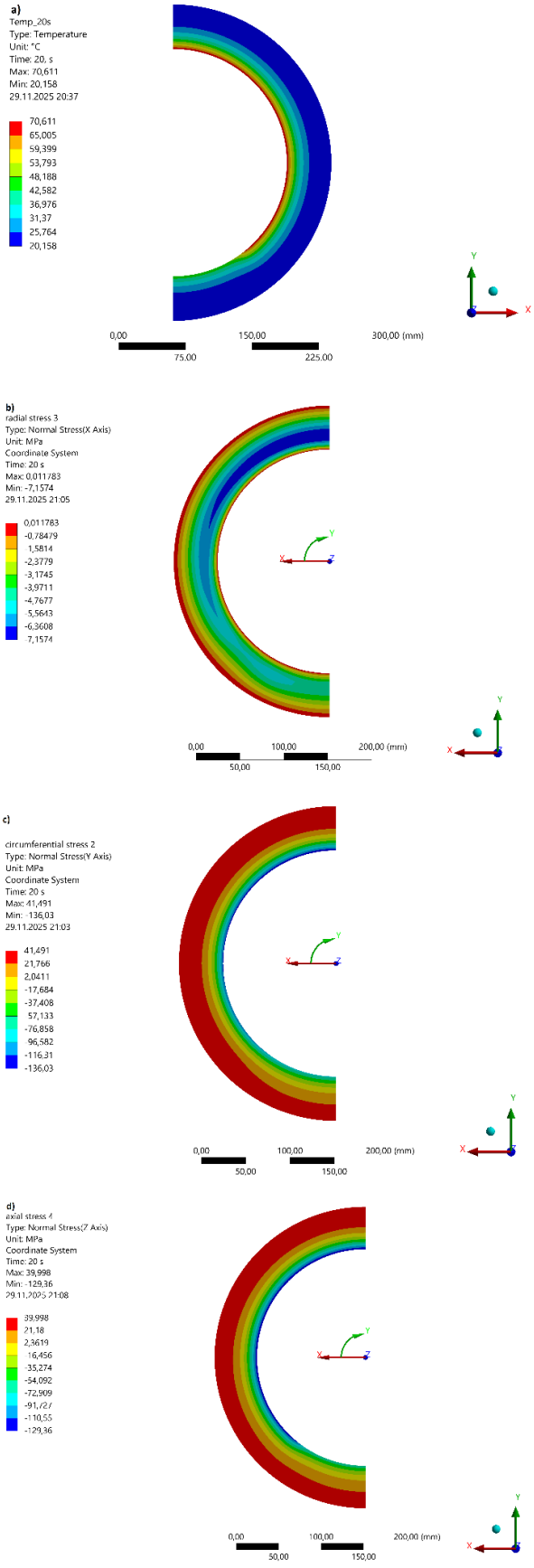

Fig. 16. Temperature and stress distribution in the middle of the header cross-section: a) temperature, b) radial stresses, c) circumferential stresses, d) axial stresses

The temperature field in Fig. 16(a) confirms that the upper part of the header is hotter than the lower part. The thermal stresses in the header cross-section are caused primarily by the temperature gradient through the wall thickness, with a smaller contribution from the circumferential temperature difference. Radial stresses are much lower than the circumferential and axial stresses (Fig. 16(b)). Considerably larger compressive stresses occur near the inner surface, while tensile stresses appear near the outer surface (Figs. 16(c) and 16(d)). The maximum circumferential tensile stress is 41.49 MPa, whereas the largest compressive stress magnitude is 136.03 MPa. Thus, the tensile stresses on the outer surface are roughly three times smaller in absolute value than the compressive stresses close to the inner surface. The axial-stress distribution follows the same pattern: the maximum tensile stress is 39.99 MPa, and the maximum compressive stress magnitude is 129.36 MPa.

5. CONCLUSIONS

This study proposes a method for monitoring temperature and stress distributions in the cross-section of a horizontal pressure header. Circumferential wall-temperature measurements taken a few millimetres below the inner surface are used to reconstruct the inner-surface temperature and heat flux. When the fluid temperature is measured, the heat transfer coefficient distribution on the internal surface can also be obtained. The method was verified numerically. First, artificial measurement data were generated by solving the transient direct heat conduction problem for a step change in fluid temperature from 20 to 100 degrees Celsius and for different inner-surface HTC values, with the outer surface treated as thermally insulated. Header temperatures 5 mm below the inner wall served as the measurement data. These data were then used to reconstruct the transient inner-surface temperature. After the complete cross-sectional temperature field had been obtained, the corresponding thermal-stress distribution was calculated. The tests show that wall-temperature measurements 5 mm from the inner surface are sufficient to reproduce the un-steady inner-wall temperature and the thermal-stress field across the whole header cross-section with very high accuracy. The proposed approach can therefore be applied for online monitoring of temperature and thermal stresses in headers. Knowledge of the time history of thermal stresses during start-up and shutdown also enables continuous assessment of fatigue-related durability loss in the pressure header.

NOMENCLATURE

c	specific heat capacity. $Jkg^{-1}K^{-1}$
h_s	heat transfer coefficient in the region of steam. $Wm^{-2}K^{-1}$
h_w	heat transfer coefficient in the region of steam. $Wm^{-2}K^{-1}$
k	thermal conductivity. $Wm^{-1}K^{-1}$
M	number of nodes in radial direction
N	number of nodes in circumferential direction
r	radial coordinate. m
r_{in}	inner radius. m
r_{out}	outer radius. m
$\dot{q}_i$	heat flux at the *i*-th node on the inner surface. Wm^{-2}
t	time. s
T	temperature. °C
β	angle. rad
Δr	finite volume thickness. m
Δt	Time step. s
γ	angle defining the water level in the header. rad
κ	thermal diffusivity. m^2s^{-1}
φ	angular coordinate. rad

REFERENCES

1. Taler J, Trojan M, Dzierwa P, Kaczmarski K, Węglowski B, Taler D, et al. The flexible boiler operation in a wide range of load changes, considering the strength and environmental restrictions. Energy. 2023;263:125745. https://doi.org/10.1016/j.energy.2022.125745
2. Gonzalez-Salazar MA, Kirsten T, Prchlik L. Review of the operational flexibility and emissions of gas- and coal-fired power plants in a future with growing renewables. Renew Sustain Energy Rev. 2018;82:497–1513. https://doi.org/10.1016/j.rser.2017.05.278
3. Skjervold V, Nord LO. Thermal energy storage integration for increased flexibility of a power plant with post-combustion CO2 capture Appl Therm Eng. 2024;246:122907. https://doi.org/10.1016/j.applthermaleng.2024.122907
4. Skjervold V, Mondino G, Riboldi L, Nord LO. Investigation of control strategies for adsorption-based CO2 capture from a thermal power plant under variable load operation. Energy. 2023;268:126728. https://doi.org/10.1016/j.energy.2023.126728.
5. Trojan M, Taler D, Dzierwa P, Taler J, Kaczmarski K, Wrona J. The use of pressure hot water storage tanks to improve the energy flexibility of the steam power unit. Energy. 2019;173:926–936. https://doi.org/10.1016/j.energy.2019.02.059
6. Stevanovic VD, Petrovic MM, Milivojevic S, Ilic M. Upgrade of the thermal power plant flexibility by the steam accumulator. Energy Convers Manag. 2020;223:113271. https://doi.org/10.1016/j.enconman.2020.113271
7. Taler J, Dzierwa P, Taler D. Optymalizacja nagrzewania i ochładzania grubościennych elementów kotłów. Procesy cieplne i przepływowe w dużych kotłach energetycznych. Warszawa: Wydawnictwo Naukowe PWN; 2011: 584-637.
8. Taler J, Dzierwa P, Taler D, Jaremkiewicz M, Trojan M. Monitoring of thermal stresses and heating optimization including industrial applications. New York: Nova Science Publishers; 2016: 245.
9. Taler J, Węglowski B, Zima W, Grądziel S, Zborowski M. Analysis of Thermal Stresses in a Boiler Drum During Start-Up. J Press Vessel Technol. 1999;121:84-93.
10. Rabazzi SM, Albanesi AE, Ramos Nervi JE, Signorelli JW. Highly detailed structural integrity assessment of the reactor pressure vessel nozzle of Atucha-I during a pressurized thermal shock event. Nucl Eng Des. 2024;418:112905. https://doi.org/10.1016/j.nucengdes.2024.112905
11. AD-Merkablatter. 2001 Taschenbuch-Ausgabe. Koln/Berlin: Carl Heymanns/Beuth; 2001: 684.
12. Jawad MH. Stress in ASME Pressure Vessels, Boilers and Nuclear Components. New York: John Wiley & Sons - ASME Press; 2018.
13. Taler D. Numerical Modelling and Experimental Testing of Heat Exchangers. Switzerland: Springer International Publishing AG; 2019.
14. Taler J, Duda P. Solving Direct and Inverse Heat Conduction Problems. Berlin: Springer; 2006.

Dawid Taler https://orcid.org/0000-0003-4341-8223

Marek Węglarz: https://orcid.org/0009-0004-4724-7980

Katarzyna Węglarz: https://orcid.org/0000-0001-8782-3760

Jan Taler: https://orcid.org/0000-0002-6717-5599

Piotr Dzierwa: https://orcid.org/0000-0001-6381-5627